Synthesis of SnO_2/B-P codoped g-C_3N_4 nanocomposites as efficient cocatalyst-free visible-light photocatalysts for CO_2 conversion and pollutant degradation

Fazal Raziq, Yang Qu, Muhammad Humayun, Amir Zada, Haitao Yu, Liqiang Jing*

Key Laboratory of Functional Inorganic Material Chemistry (Heilongjiang University), Ministry of Education, School of Chemistry and Materials Science, International Joint Research Center for Catalytic Technology, Harbin 150080, PR China

ARTICLE INFO

ABSTRACT

Coping with the gradually increasing worldwide environmental issues, it is highly desired to develop efficient, cheap and visible-light responsive nano-photocatalysts for CO_2 conversion and pollutant degradation. Herein, we have successfully synthesized SnO_2-coupled boron and phosphorus co-doped g-C_3N_4 (SO/B-P-CN) nanocomposites as efficient cocatalyst-free visible-light photocatalysts of low cost for both CO_2 conversion and pollutant degradation. It is shown that the amount-optimized SO/B-P-CN nanocomposite exhibits enhanced visible-light activities for CO_2 conversion to CH_4 from CO_2-containing water by ~9 times, and for phenol and acetaldehyde degradation by ~7 times, as compared to the bare CN nanosheets. Moreover, it is confirmed that a large amount of produced hydroxyl radicals on SO/B-P-CN is well responsible for the greatly-enhanced photocatalytic activities. Interestingly, the evaluated quantum efficiency (2.02%) of optimized SO/B-P-CN nanocomposite for photocatalytic CO_2 conversion at λ=420 nm is much higher than other reported result. Mainly based on the surface photovoltage responses and the photocurrent action spectra, it is suggested that the enhanced activity of SO/B-P-CN nanocomposite depends on the extended visible-light absorption from 460 to 550 nm after B-P co-doping, and the promoted charge separation via the dopant-induced surface states and the coupled SO nanoparticles. This work implies that the modified CN nanosheets as cheap nanocomposites display promising applications in the photocatalytic field of CO_2 conversion to useful fuels and pollutant degradation for environmental remediation.

© 2016 Elsevier B.V. All rights reserved.

1. Introduction

It is well known that carbon dioxide (CO_2), mostly generated from combustion of fossil fuels and vehicle exhaust, is one of the major contributors to the green-house gases, leading to severe environmental problems, such as melting glaciers, rising sea levels, and increased floods [1,2]. Accordingly, extensive research has been directed toward CO_2 conversion into energy rich compounds with the help of traditionally complex electrolytic and biological methods [3]. Similarly, organic contaminants are also serious problems in industrial wastewater discharges, consequently giving rise to various environmental pollution, even normally non-biodegradable and potentially carcinogenic [4]. General technologies used in the treatment of industrial wastewater include activated carbon adsorption, solvent extraction, and O_3-related chemical oxidation, which easily produce secondary pollution and even much hazardous byproducts. However, heterogeneous semiconductor photocatalysis, as a promising alternative technology for CO_2 conversion into useful fuels, such as CH_4, CO, and CH_3OH, and pollutant degradation into CO_2, H_2O and other inorganic substances, has attracted much attention because of its low cost, high efficiency, and solar energy utilization [5,6]. Based on the large proportion of visible light content in the solar radiation, it is much meaningful to develop a stable, cheap, and efficient photocatalyst to utilize under visible-light irradiation.

Compared to the widely-investigated various metal-containing visible-light photocatalysts, such as oxide, sulfide and oxynitride [7], a metal-free polymeric semiconductor, graphitic carbon nitride (g-C_3N_4), has been regarded as a highly potential photocatalytic material in recent years for CO_2 reduction, pollutant degradation, and H_2 evolution under solar light irradiation because of its low cost, unique chemical stability, environmentally benign and tun-

able microstructure [8]. Unlike metal sulfide and oxynitride, it is stable under light irradiation in aqueous, acidic (HCl, pH = 0) and basic (NaOH, pH = 14) solutions due to the strong covalent bonds between C and N-atoms [9]. Besides, it possesses an appropriate microstructure with alternate N atoms with lone pair of electrons for anchoring active sites [10]. Due to these superior properties, g-C_3N_4 (CN) has become the focus in the photocatalysis field nowadays. However, it still exhibits unsatisfactory photocatalytic performance from the theoretical and practical points of view. This is mainly attributed to its limited visible-light absorption and high charge recombination [11]. Therefore, it is highly desired to greatly improve the photoactivity of CN by expanding its visible-light absorption and enhancing its charge separation.

CN exhibits an energy bandgap of 2.7 eV, corresponding to 459 nm light threshold, indicating that it has a limited visible-light absorption range. Its conduction band (CB) bottom and valence band (VB) top are respectively located at −1.3 and 1.4 eV potentials via NHE [12]. It is possible to expand the visible-light response of CN by properly altering the CB bottom downward and the VB top upward. For this, doping nonmetals, such B, P and S, could expand the visible-light response by affecting the electronic properties so as to improve the photoactivities [13,14], although the really effective absorption threshold and the effects of introduced dopants as formed surface states on the charge separation are always neglected. As a result, the activity-enhanced mechanisms are not fully understood. In our recent work [15], it is demonstrated that boron doping in CN could enhance the photocatalytic activity for degrading pollutants. Thus, it is much feasible to co-dope B and P into CN for efficient visible-light photocatalysis, with great significance by deeply revealing the mechanisms. Unfortunately, few related works have been reported to date.

In order to suppress the high charge recombination, several strategies have been worked out to modify CN, including preparation of different nanostructures, deposition of stable and visible-light active metals, protonation and coupling other nano-sized semiconductor oxides to form hybrids [16–19]. Among those strategies, the coupling of wide-bandgap oxides has been taken as a simple and effective modification method. Compared with the widely-used TiO_2 and ZnO, tin oxide (SO) as a wide-bandgap (3.5 eV) semiconductor has seldom been employed to modify CN [3]. It has potential applications in solar cells, catalytic support materials, transparent electrodes, and solid-state chemical sensors owing to its outstanding electrical, optical, and electrochemical properties. However, the CB bottom of SO lies at 0.04 eV vs NHE [20], which is unfavorable to induce reduction reactions thermodynamically. It is possible that after coupling to CN, the CB level of SO at the interface will slightly move upward due to band bending [13]. In this case, the transferred electrons from CN could energetically initiate the reduction reactions. Thus, it is expected that it is much meaningful to utilize nano-sized SO to modify CN with a great possibility for efficient visible-light photocatalysis.

Photocatalytic reactions for both CO_2 reduction and pollutant degradation are usually involved with a series of photophysical and photochemical processes [21]. Among these processes, the separation as the main photophysical process of photogenerated charges and the production as the main photochemical intermediates of hydroxyl radicals (•OH) are much crucial for efficient photocatalytic processes [22]. Hence, it is much meaningful to deeply understand the mechanism of photocatalytic reactions and to investigate the separation of photogenerated charges and the production of •OH intermediate. It has been well developed in our group that the surface photovoltage technique, especially for the atmosphere-controllable one, is an effective testing method with high sensitivity to investigate the photogenerated charge separation properties [23]. To the best of our knowledge, there have been no reports on the efficient cocatalyst-free visible-light CN-based photocata-

lysts for CO_2 conversion and pollutant degradation by co-doping B and P, and then coupling SO, along with the detailed photocatalytic mechanisms until now. This work will help to understand the photophysics- and photochemistry-related mechanisms in detail, and provide feasible routes to design visible-light nanostructured CN-based photocatalysts for efficient solar energy utilization to solve environmental issues.

2. Experimental section

2.1. Synthesis of materials

All the reagents were of analytical grade and used as-received without further purification. Deionized water was used throughout the reaction.

2.1.1. g-C_3N_4 (CN) nanosheets
CN nanosheets were obtained simply by the calcination of dicyandiamide (DCDA) [24]. In a typical experiment, 20 g of dicyandiamide was taken in a ceramic crucible and heated in a muffle furnace at 550 °C (5 °C min^{-1}) for 4 h. After that, the material was cooled to room temperature, grinded into powder and re-calcined at 550 °C for 3 h to obtain CN nanosheets.

2.1.2. Boron and phosphorus Co-doped CN nanosheets (B-P-CN)
B and P co-doped CN nanosheets (B-P-CN) were synthesized using ionic liquids [25]. In a typical synthesis, a certain amount of 1-butyl-3-methyl imidazolium-tetra-fluoroborate (BmimBF4) as a boron and 1-butyl-3-methyl imidazoliumhexafluorophosphate (BmimPF6) as a phosphorus source were dissolved in 25 mL water and stirred for 30 min. After that, 2 g of DCDA was added to the mixture and heated at 100 °C in an oil bath until water was completely evaporated and hard solid was left. The resulting white solid was milled and heated in a ceramic crucible at 350 °C (2 °C min^{-1}) for 2 h. Simultaneously, the temperature was raised to 550 °C (5 °C min^{-1}) and kept at this temperature for 4 h. After cooling to room temperature, the material was milled and re-calcined at 550 °C for 3 h to obtain XB-YP-CN nanosheets, in which X and Y respectively represent the mass ratio percentage of B and P to CN.

2.1.3. Synthesis of SnO_2 (SO) nanoparticles
In a typical synthesis, 2 g of $SnCl_4 \cdot 5H_2O$ was dissolved in deionized water and then a desired amount of NaOH solution was dropwise added to it under continuous stirring. At the beginning, a white cloudy suspension was formed in the acidic pH range, while it slowly disappeared with the addition of more NaOH solution. After the pH value reached to 12, that solution became transparent. Subsequently, 60 mL of the obtained solution was transferred into a 100 mL Teflon-lined stainless steel autoclave and hydrothermally treated at 200 °C for 12 h. After cooling to room temperature naturally, the obtained product was washed 3 times with distilled water to remove impurities and then dried at 60 °C in an oven overnight, SO nanoparticles were obtained.

2.1.4. SnO_2 (SO)/B-P-CN nanocomposites
To fabricate SO/B-P-CN nanocomposites, for each sample 2 g freshly prepared 0.12B-0.20P-CN powder was taken and dissolved into a mixed solution of 5 mL distilled water and 20 mL ethanol. The mixture was kept under vigorous stirring for 2 h. After that, different mass ratio percentage (4, 6, 8%) of SO was added to each sample and the mixture was kept under continuous magnetic stirring for 2 h. Subsequently, the mixture was dried in oven at 80 °C and finally calcined at 500 °C for 2 h. Thus, ZSO/B-P-CN nanocomposites were obtained, in which Z represents different mass ratio percentage of SO coupled.

2.2. Characterization of materials

X-ray powder diffraction (XRD) measurements of all samples were carried out with XRD (Bruker D8, Germany), using Cu Kα radiation (α = 0.15418 nm), at an accelerating voltage of 30 kV while emission current of 20 mA was employed. Electron micrographs were taken on a JEOL JEM-2010 transmission electron microscope (TEM) operated at 200 kV. In order to probe various bonds and impurities in samples, Fourier transform infrared (FT-IR) spectra were obtained in the range of 400–4000 cm^{-1} using KBr as a diluent. The compositions and elemental chemical states of all samples were checked through X-ray photoelectron spectroscopy (XPS) using a Kratos-Axis Ultra DLD apparatus with an Al (mono) X-ray source. The binding energies mentioned in this paper were calibrated with respect to the signal for adventitious carbon (binding energy = 284.6 eV). The presence of B or P was confirmed with the help of Bruher nuclear magnetic resonance (NMR) serial no 00067 (model 2014) instrument. The UV–vis diffuse reflectance spectra (DRS) of the samples were measured with a Shimadzu UV-2550 spectrometer. The photoluminescence (PL) spectra of the samples were measured with a PE LS 55 spectrofluoro-photometer at excitation wavelength of 390 nm.

The atmosphere-controlled steady-state surface photovoltage spectroscopy (SS-SPS) measurements of the samples were carried out with a home-built apparatus,[33] equipped with a lock-in amplifier (SR830) synchronized with a light chopper (SR540).The powder sample was sandwiched between two indium-tin-oxide (ITO) glass electrodes kept in an atmosphere-controlled sealed container. A monochromatic light was obtained from 500 W xenon lamp (CHF XQ500W, Global xenon lamp power) through a double prism monochromator (SBP300).

2.3. Photoelectrochemical (PEC) measurements

To study the photoelectrochemical performance, following experiments were performed. For each sample 0.05 g powder was taken and dispersed in 2 mL isopropyl alcohol under vigorous magnetic stirring for 1 h. Then 0.025 g Macrogol-6000 was added to each sample and ultrasonically treated for 30 min, followed by continuous magnetic stirring for 1 h. At last, 0.05 mL acetyl acetone was added to the reaction mixtures and kept under vigorous magnetic stirring for 72 h. The conductive fluorine doped tin oxide (FTO) coated glasses were cleaned by ultrasonication in acetone for 2 h and then washed with deionized water and ethanol in turn. After drying in air for 20 min, the cleaned FTO coated glasses were used as substrates for CN, XP-CN, YB-0.2P-CN, and ZSO/0.12B-CN0.20P-CN samples. Thin films of all samples were prepared by doctor blade method using Scotch tape as a spacer. The prepared films were dried in air for 30 min and then calcined at 450 °C for 30 min. The FTO coated glasses with thin film were cut into 1.0 cm × 3.0 cm pieces having film surface area 1.0 cm × 1.0 cm. To prepare photoelectrode, an electrical contact was made with the FTO substrate by using a silver conducting paste connected to a copper wire and then enclosed in a glass tube. The working arithmetic surface area of the film on FTO was 0.5 cm × 0.5 cm while the remaining area was covered with epoxy resin.

2.4. Evaluation of produced •OH amount

Hydroxyl radical measurement was carried out in 0.001 M coumarin aqueous solution in a quartz reactor of 40 mL containing 0.05 g of sample powder. Prior to irradiation, the reactor was magnetically stirred for 10 min to attain an adsorption-desorption equilibrium. After irradiation for 1 h, the sample was centrifuged and a certain amount was transferred into a Pyrex glass cell for the fluorescence measurement of 7-hydroxycoumarin at 390 nm exci-

tation wavelength and emission wavelength at 460 nm through a spectrofluorometer (Perkin-Elmer LS55).

2.5. Evaluation of photocatalytic activities for CO$_2$ conversion

In the photocatalytic reduction of CO$_2$, for each experiment, 0.2 g powder sample was dispersed in water (3 mL)/NaOH contained in a cylindrical steel reactor with 100 mL volume and area 3.5 cm^2. A 300W Xenon arc lamp was used as the light source with a cut-off filter of 420 nm for the photocatalytic reaction. High pure CO$_2$ gas was passed through water and then entered into the reaction setup for reaching ambient pressure. The used photocatalyst was allowed to equilibrate in the CO$_2$/H$_2$O system for 1 h. During irradiation, about 0.5 mL of gas was continually taken from the reaction cell at given time interval for the analysis of CH$_4$ concentration using a gas chromatograph (GC-2014 with FID detector; Shimadzu Corp., Japan). The isotopic experiments for ^{13}CO$_2$ reduction were performed with GC-7890B/MS5977A (America Aligent).

2.6. Evaluation of photocatalytic activity for pollutant degradation

The photocatalytic activities of the samples were evaluated by selecting liquid phase phenol and gas phase acetaldehyde as model pollutants, because of their existence as by-product in industrial synthesis and harmful effects to both human health and natural environment. The degradation of acetaldehyde was carried out in a 640 mL cylindrical quartz reactor, irradiated with 150 W (GYZ220) high-pressure Xenon lamp made in China, whose emitting spectrum is similar to sunlight. To cutoff UV-light, a light filter of 420 nm was placed between the light source and the reactor. In a typical experiment, 0.1 g of photocatalyst was introduced into the reactor, in which a gas system containing 810 ppm of acetaldehyde, 20% of O$_2$, and 80% of N$_2$ was pre-mixed. Prior to irradiation, the reactor containing mixed gases was kept for 30 min in dark to reach adsorption-desorption equilibrium. The concentration of acetaldehyde was measured at 30 min intervals with a gas chromatograph (GC-2014, Shimadzu) equipped with a flame ionization detector.

The photocatalytic experiment for phenol degradation was carried out in a 100 mL glass reactor and the radiation source was a 150 W GYZ220 high-pressure Xenon lamp (made in China) with a cut-off filter of 420 nm. To measure the photocatalytic activity, for each measurement 0.1 g of photocatalyst was taken and mixed with 80 mL of 10 mg/L phenol solution under stirring for 1 h to reach adsorption saturation and then irradiated for 1 h. After irradiation for 1 h, the samples were centrifuged and phenol concentration was analyzed by the colorimetric method of 4-aminoantipyrine at the characteristic optical adsorption of 510 nm with a Model Shimadzu UV2550 spectrophotometer [26].

3. Results and discussion

3.1. Structural characterization and surface composition

The crystalline structures of as-prepared samples were investigated by X-ray diffraction (XRD) patterns, as shown in Fig. 1Aand Fig. S1. Generally, it is accepted that CN is based on tri-s-triazine building blocks. The intense peak at 27.41° is the characteristic peak for interlayer stacking aromatic systems, indexed for graphitic materials at (002) facet. The calculated inter-planar distance for aromatic units (d = 0.325 nm) are considerably smaller than that of crystalline CN (d = 0.34 nm) [27]. After doping phosphorus, the peak at 27.41° is slightly shifted toward the lower 2θ value, suggesting that phosphorus is successfully incorporated in the triazine ring, as shown in Scheme. S1 [28]. In contrast, when B and P are simultaneously co-doped in CN, the same peak is a little shifted toward higher
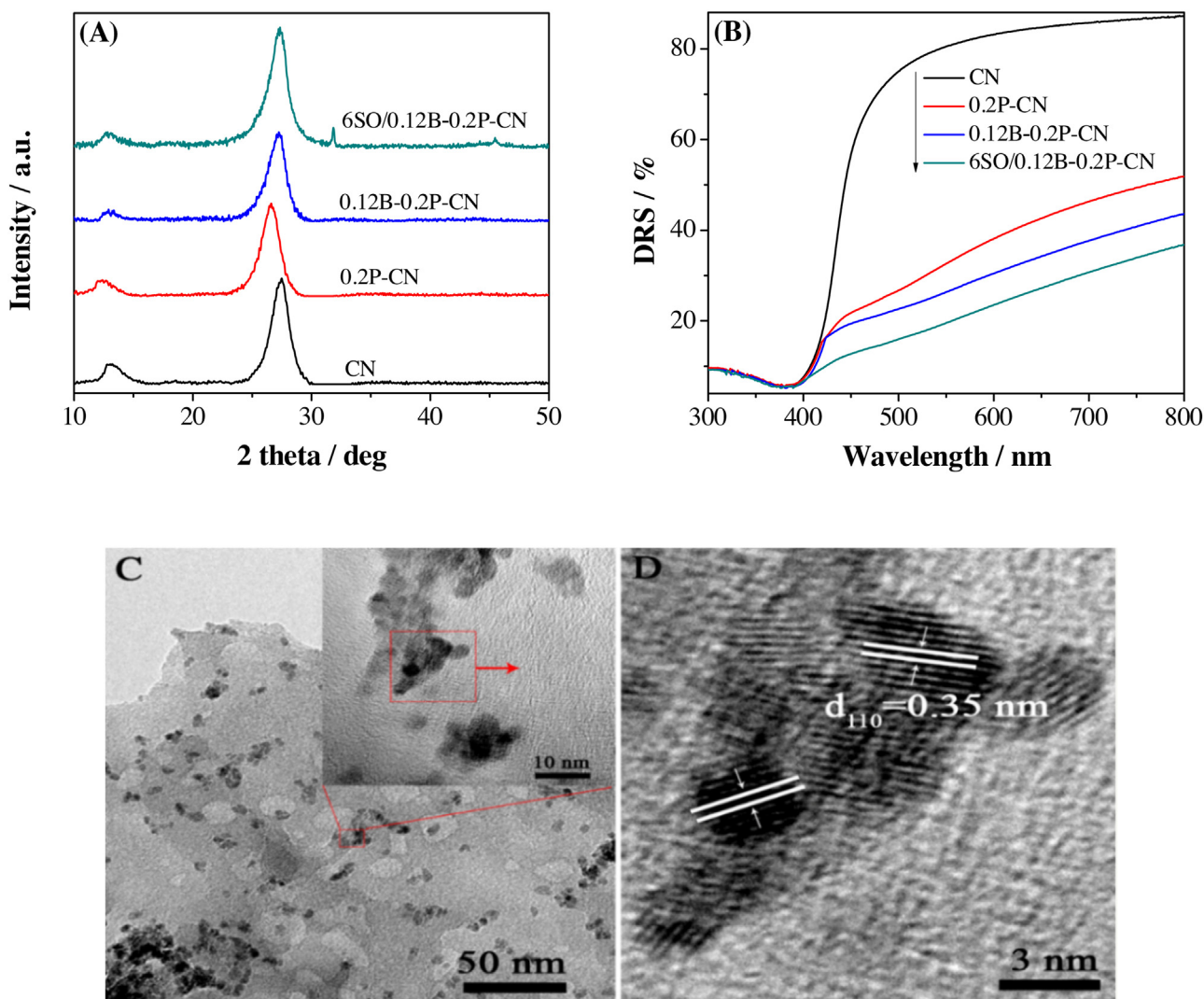
Fig. 1. XRD patterns (A) and UV–vis diffuse reflectance spectra (B) of CN, 0.2P-CN, 0.12B-0.2P-CN and 6SO/0.12B-0.2P-CN samples. TEM (C) and HRTEM (D) micrographs of 6SO/0.12B-0.2P-CN nanocomposite.

2θ value due to the smaller radius of boron. The weak peak at 32.5° is attributed to the characteristic peak of coupled nanocrystalline SO. However, it is clear that coupling SO does not alter the crystal phase of B-P co-doped CN samples.

To examine the optical absorption behavior of the resultant CN, XP-CN, YB-0.2P-CN and ZSO/0.12B-0.2P-CN samples, the UV–vis diffuse reflectance spectra (DRS) were recorded. From the UV–vis diffuse reflectance spectra (Fig. 1B and Fig. S2), it is clear that P and B co-doping can greatly extend the absorption of CN toward visible range. Hence, less energy is needed to excite the electrons from the VB of CN to its CB. Further, it is noticed that coupling different mass ratio percentages of SO could be favorable for the visible-light absorption of B-P-CN to a certain degree. The TEM and HRTEM micrographs of 6SO/0.12B-0.2P-CN sample are shown in Fig. 1C and D, respectively. It is clear that SO nanoparticles are uniformly dispersed on the surfaces of 0.12B-0.2P-CN sample, and the heterojunctions are formed since the lattice fringes at inter-planar distance 0.35 nm is attributed to SO. Hence, it is expected that the formed heterojunction is much favorable for the transfer and the separation of photogenerated charges.

To further confirm the functional groups and chemical species of as-prepared samples, fourier transform infrared (FTIR) spectra were measured, as shown in Fig. 2A. The stretching modes of C—N heterocycles at 1200–1600 cm⁻¹, along with the vibration peak at 812 cm⁻¹, are attributed to the characteristic absorption peaks of triazine units. The peaks at 3000–3600 cm⁻¹ are ascribed to the stretching vibration mode of N—H bond in CN, as well as the surface-adsorbed OH groups. A small peak for N-P at 852–950 cm⁻¹ is detected, which is consistent with the previous report [29]. However, the vibrations of Boron-related groups are hardly observed. In order to confirm the elemental chemical states, X-ray photoelectron spectra (XPS) were measured, as shown in Fig. 2B, C and Fig. S3. The N1 s XPS spectra of CN, 0.2P-CN, 0.12B-0.2P-CN and 6SO/0.12B-0.2P-CN are fitted into three contributions according to the Gaussian rule with origin software. These contributions located at 398, 400 and 401 eV respectively, are attributed to the aromatic nitrogen atoms bonded to sp² hybridized carbon atom (C—N═C) [39], tertiary nitrogen groups N—(C)₃ connecting structural motif or ((C)₂—N—H) groups inter-linked with structural defects, and nitrogen atoms bonded with two carbon atoms in the aromatic rings. It is clear that the binding energy of N1s for B—P co-doped CN sample is slightly shifted toward lower binding energy. The XPS spectra of C1s are fitted into two components located at 284.6 and 287.2 eV. The former at 284.6 eV is ascribed to the C—C bond originated from sp²C atoms bonded to N atoms in the aromatic cycle (N—C═N), while the later at 287.2 eV corresponds to C═N. Like N, the binding energy
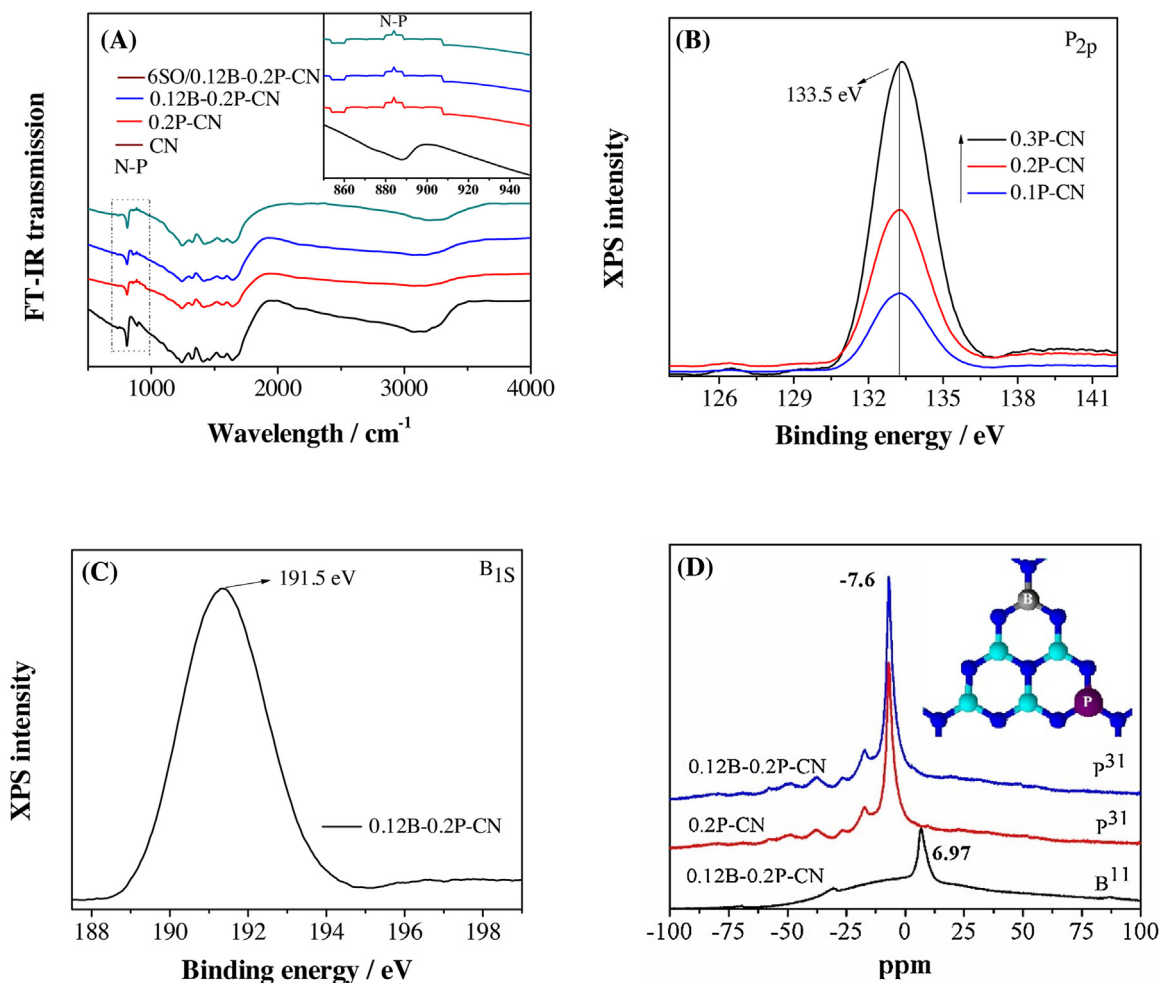
Fig. 2. FT-IR spectra of CN, 0.2P-CN, 0.12B-0.2P-CN and 6SO/0.12B-0.2P-CN (A). P2p XPS (B) of 0.1P-CN, 0.2P-CN and 0.3P-CN, and B1s XPS of 0.12B-0.2P-CN (C). NMR spectra of boron and phosphorus (D) of 0.2P-CN and 0.12B-0.2P-CN.

of carbon (C−N) is also shifted towards low energy side due to the electron delocalization effect [30]. The binding energy of B1 s is centered at 191.5 eV, which is slightly higher than the binding energy of h-BN (190.0 eV) and lower than that of Kawaguchi's boron carbon nitride BCN(H) (192.1 eV, in which boron is surrounded by three nitrogen atoms). Thus, it is concluded that a boron atom is doped into CN with different amounts by substituting C, which is consistent with the reported work [31]. In addition, the binding energy of P2p in phosphorus doped CN is located at 133.5 eV, which is typical for a P-N coordination, while that of pristine $g-C_3N_4$ naturally only shows negligible contributions. In addition and most relevant, no fluorine could be detected in the final material [32]. Hence, it is suggested that B and P are successfully incorporated into the CN lattice by substituting C atoms. It was demonstrated that phosphorus heteroatoms most probably replaced the corner or bay carbon to form P–N bonds in the phosphorus doped CN framework [28], and P was attached with three nitrogen atoms in the ring based on the first-principle density functional theory [33].

To further confirm the position of B and P in the co-doped structure, Nuclear Magnetic Resonance (NMR) measurements were performed, as shown in Fig. 2D. The obvious peak at 6.97 ppm is attributed to B in the 0.12B-0.2P-CN sample, while the four well-resolved signals between 0 and −50 ppm mean four different positions of P in the CN framework. Hence, it is deduced that P elements in the 0.2P-CN replace the corner or bay carbon in the framework to form P-N bonds [25]. Moreover, the intense peak at −7.6 ppm in 0.2P-CN is slightly shifted toward positive side in

0.12B-0.2P-CN sample. Based on the NMR analysis, it is confirmed that B and P are successfully co-doped in the triazine ring of CN [34].

3.2. Visible-light activities for CO_2 reduction and pollutant degradation

The visible-light photocatalytic activities of CN, XP-CN, YB-0.2P-CN and ZSO/0.12B-0.2P-CN samples were evaluated for CO_2 reduction in water without any co-catalyst. From Fig. 3A and Fig. S4, it can be seen that CN exhibits weak photocatalytic activity for CO_2 conversion to CH_4 (~5.7 μmol) after 8 h irradiation. It is obvious that P-CN samples exhibit the enhanced visible-light activities for CO_2 conversion, and the highest activity (18 μmol) is observed for 0.2P-CN one. After continuously doping boron into the optimized 0.2P-CN, the visible-light activity for CO_2 conversion is further enhanced, especially for 0.12B-0.2P-CN (37 μmol) with a proper amount of B. Moreover, it is confirmed that the activity of 0.12B-0.2P-CN is significantly enhanced after coupling different mass ratio percentages of SO nanoparticles, and the highest activity is observed for 6SO/0.12B-0.2P-CN (49 μmol), with 9-time enhancement compared to the pure CN. Noticeably, the visible-light photocatalytic activity for CO_2 conversion in NaOH (pH = 10) is higher than that in water, which is attributed to the increased dissolution of CO_2 in the presence of NaOH. Meanwhile, we have also measured the photoactivities of XP-CN under UV–vis light, as shown in Fig. S4B. It can be seen that the photoactivity under
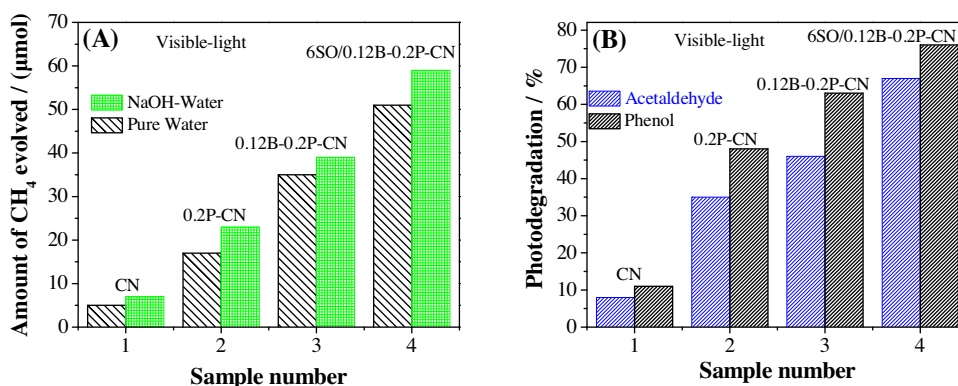
Fig. 3. Activities for CO_2 conversion in pure water and in NaOH solution for 8 h (A), and for acetaldehyde and phenol degradation (B) of CN, 0.2P-CN, 0.12B-0.2P-CN and 6SO/0.12B-0.2P-CN under visible-light irradiation.

UV–vis light is twice as compared to that of visible-light one. Interestingly, the calculated quantum efficiencies under visible-light irradiation (at λ=420 nm) for CO_2 reduction of 0.2P-CN, 0.12B-0.2P-CN and 6SO/0.12B-0.2P-CN are respectively 1.35%, 1.93% and 2.02%, relatively higher than that in other reported work (0.9%) [35]. Moreover, this work also exhibits a much large field of CH_4 in the photocatalysis compared with other works [36–38].

It is necessary to confirm that the produced CH_4 comes from CO_2 reduction rather than C_3N_4 decomposition. For this, we have mainly tried to complete two confirmatory tests. Firstly, we have performed the blank photocatalytic experiment without any CO_2 in N_2 on C_3N_4 under the same condition. After irradiation for 4 h, we have not detected any fuels. Secondly, we have carried out an isotopic experiment by using $^{13}CO_2$ under the identical photocatalytic reaction condition. The photocatalytic products were analyzed by a gas chromatography-mass spectrometry (GC–MS) apparatus. As shown in Fig. S5, after visible-light irradiation for 8 h, the detected isotopic peak at $m/z = 17$ is assigned to $^{13}CH_4$, and the detected other peaks at $m/z = 13$, 14, 15, and 16 are respectively attributed to the fragments of $^{13}CH_4$. We have also observed the peaks for N_2 ($m/z = 28$) as the dilute agent, for ^{13}CO ($m/z = 29$) as the fragment of $^{13}CO_2$, for O_2 ($m/z = 32$) as the photocatalytic production, and for $^{13}CO_2$ ($m/z = 45$) as the raw material. In addition, it had been demonstrated that the g-C_3N_4 based photocatalysts for photocatalytic CO_2 reduction could be stable under visible-light irradiation [39–41]. Thus, it is confirmed that the produced CH_4 comes from CO_2 via the photocatalytic reactions, with simultaneous production of O_2.

To further prove the enhanced photoactivities, we have measured the visible-light photocatalytic degradation of acetaldehyde and phenol on CN, 0.2P-CN, 0.12B-0.2P-CN and 6SO/0.12B-0.2P-CN, as shown in Fig. 3B. It is obvious that CN exhibits low photocatalytic activity. As expected, the visible-light photocatalytic activities could be enhanced after doping P (0.2P-CN), especially for that co-doped with P and B (0.12B-0.2P-CN). Interestingly, the resulting 6SO/0.12B-0.2P-CN nanocomposite exhibits the highest photoactivity by 7-time enhancement, compared with the bare CN. Therefore, it is confirmed that the visible-light photocatalytic activity of CN could be greatly enhanced by co-doping P and B, and then coupling to nanocrystalline SO.

3.3. Photophysical and photochemical properties

The photoinduced electron-hole formation and separation can be analyzed directly through a highly sensitive atmosphere-controlled steady-state surface photovoltage spectroscopy (SS-SPS) measurement [42]. The SPS response for nanosized semiconductors mainly derives from the photoinduced charge separation via the diffusion process [43]. In general, the strong SPS signal corresponds to the high separation of photogenerated charges. According to Fig. 4A and Fig. S6, it is clear that CN exhibits low SPS signal in air. However, its SPS signal is obviously enhanced after doping P, and further enhanced after co-doping P and B with proper amounts, especially for 0.2P-CN and 0.12B-0.2P-CN. Interestingly, it is found that the SPS responses are significantly improved by continuously coupling nanocrystalline SO, and it is the highest for the 6SO/0.12B-0.2P-CN nanocomposite. From Fig. 4A inset, it is noticed that the SPS response range is gradually expanded to the longer-wavelength direction after co-doping P and B, and coupling SO. In addition, two points should be emphasized as follows. Firstly, the SPS response is enhanced with increasing the content of O_2, indicating that the adsorbed O_2 could effectively capture the photogenerated electrons so as to promote the charge separation. Secondly, no SPS responses for CN and P-doped CN are observed in N_2, while obvious SPS responses for 0.12B-0.2P-CN and 6SO/0.12B-0.2P-CN are seen, especially for the latter. This is attributed to the roles of B-induced surface states to capture the photogenerated holes and that of coupled SO nanoparticles to accept the transferred electrons [44]. Thus, from the above SPS results, it is deduced that the photogenerated charge separation of CN could be greatly enhanced by co-doping P and B, and then coupling with nanocrystalline SO, along with its visible-light extension.

To investigate the photogenerated charge recombination properties of as-prepared samples, PL spectra were measured at the excitation wavelength of 390 nm [45], as shown in Fig. 3B, and S7. It is found that CN exhibits a strong PL signal centering at about 460 nm. The energy of this PL signal is closely associated with the optical bandgap energy of the CN (2.7 eV), according to the widely-accepted equation: $E_g = 1240/\lambda$ [24]. Therefore, it is confirmed that the PL signal is directly related to the band-edge emission [46]. Obviously, the PL intensity of CN is significantly decreased after doping P, and further decreased after co-doping P and B. In particular, the 0.2P-CN and 0.12B-0.2P-CN exhibit low PL signals. Interestingly, it is confirmed that the PL intensity is continuously decreased after coupling SO, and the 6SO/0.12B-0.2P-CN nanocomposite exhibits the lowest PL signal. Since the PL attribute is closely related to the band–band electronic transition, it is generally accepted that the stronger is the PL signal, the higher is the photogenerated charge recombination. Obviously, the PL results are consistent with the above SS-SPS ones. To confirm the enhanced charge separation, we have also measured the photoelectrochemical behaviors under visible-light irradiation in 0.5 M Na_2SO_4 solution, as shown in Fig. 4C. The photocurrent density of CN is greatly enhanced after doping P and then simultaneously co-doping B. It is clear that the highest photocurrent response is observed for 0.12B-0.2P-CN sample. Expectedly, after coupling
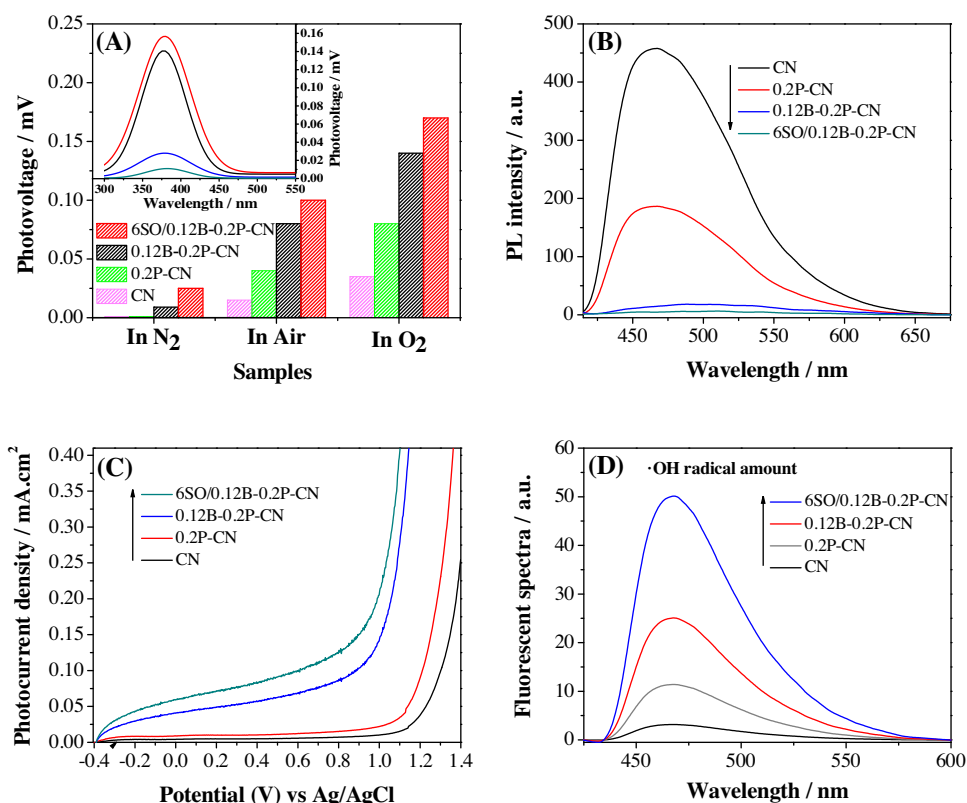
Fig. 4. SS-SPS peak intensities at different atmospheres with the SS-SPS responses in air as the inset (A), Photoluminescence spectra (B), IV-Curves (C) and Hydroxyl radical amount- related fluorescence spectra (D) of CN, 0.2P-CN, 0.12B-0.2P-CN and 6SO/0.12B-0.2P-CN samples.

nanocrystalline SO, the photocurrent density is further enhanced, and a significant enhancement is observed for the 6SO/0.12B-0.2P-CN nanocomposite. This is further supported by the obtained transient current densities under the chopped visible-light illumination at the applied voltage of 0.3 V vs Ag/AgCl electrode in 0.5 M Na_2SO_4 (Fig. S8). However, the over excess amount of coupled SO covers the photocatalyst surface and hinders the charge transfer because SO do not show any response under visible light.

To further explore the charge transfer and separation, the coumarin fluorescent method was used to detect the amount of produced hydroxyl radicals, in which the coumarin easily reacts with •OH and then produces luminescent 7-hydroxycoumarin [47]. In general, the stronger is the fluorescent signal, the larger is the produced •OH amount. The amounts of produced •OH for CN, XP-CN, YB-0.2P-CN and ZSO/0.12B-0.2P-CN samples are shown in Fig. 4D and Fig. S9. It is demonstrated that CN exhibits a low amount of •OH, while for P-CN samples, the produced •OH amounts are considerably higher, especially for 0.2P-CN. Moreover, after co-doping P and B, the produced •OH amounts are further enhanced, much obvious for 0.12B-0.2P-CN with proper amounts of P and B. Interestingly, the produced •OH amounts are remarkably increased after coupling SO nanoparticles, and the 6SO/0.12B-0.2P-CN one produced the largest amount of •OH species. Obviously, this is well consistent with the above SS-SPS, PL and PEC results.

3.4. Discussion on mechanism

To deeply reveal the related mechanisms, we have measured the photocatalytic activities for CO_2 conversion of CN, 0.2P-CN, 0.12B-0.2P-CN and 6SO/0.12B-0.2P-CN samples under the single-wavelength irradiation from 550 to 365 nm for 4 h. From Fig. 5A, it can be observed that CN shows an obvious photocatalytic activity for CO_2 conversion under the irradiation below 450 nm, while it has

a weak photoactivity at 470 nm. In contrast, it is seen that the photoactivities for 0.2P-CN and 0.12B-0.2P-CN could be displayed up to 520 nm and 550 nm, respectively. As expected, the 6SO/0.12B-0.2P-CN nanocomposite exhibits much high photoactivity up to 550 nm. This is further supported by the photocurrent action spectra measured in 0.5 M Na_2SO_4 solution under single-wavelength excitation ($\lambda \leq 600$ nm) at 0.3 V bias vs Ag/AgCl electrode (Fig. 5B). It can be observed that the photocurrent action spectrum for pure CN exhibits an obvious response below 450 nm, with a weak one upto 470 nm. This is in good agreement with the bandgap energy of CN. For 0.2P-CN and 0.12B-0.2-P-CN, the enhanced photocurrent response could appear at 520 nm and 550 nm, respectively. As expected, the 6SO/0.12B-0.2-P-CN nanocomposite exhibits the strongest photocurrent response up to 550 nm. This threshold wavelength is closely related to the electron excitation in 0.12B-0.2-P-CN with the band gap of 2.2 eV.

To well understand the improved visible-light photoactivities of CN after co-doping B and P, and then coupling nanocrystalline SO, a mechanism schematic is proposed, as shown in Fig. 6. As stated above, the visible-light absorption of CN is extended after doping with a proper amount of P. This is attributed to the formed new surface states near to the CB bottom of CN [14]. Continuously doping B, the visible-light absorption of CN is further extended, which results from the formed new surface states located near to the VB top of CN [31]. Interestingly, the formed B-related surface states could capture the photogenerated holes so as to promote the charge separation [15]. Hence, it is understandable that the visible-light absorption of CN could greatly be expanded from 460 (2.7 eV) to 550 nm (2.2 eV) by changing CB downward and VB upward to a proper degree, with the obviously enhanced charge separation, after co-doping P and B. However, if the amounts of used P and B are in excess, it is unfavorable for the charge separation since the formed surface states easily take
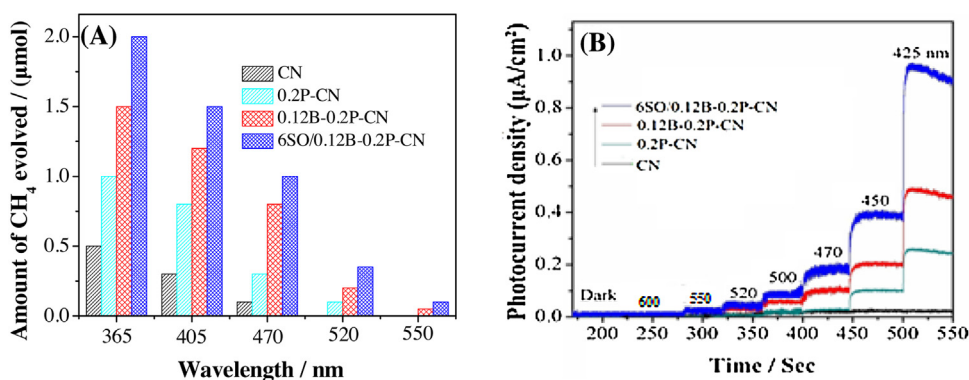
Fig. 5. Single-wavelength activities for CO$_2$ conversion (A) and single-wavelength photocurrent action spectra (B) of CN, 0.2P-CN, 0.12B-0.2P-CN and 6SO/0.12B-0.2P-CN samples.
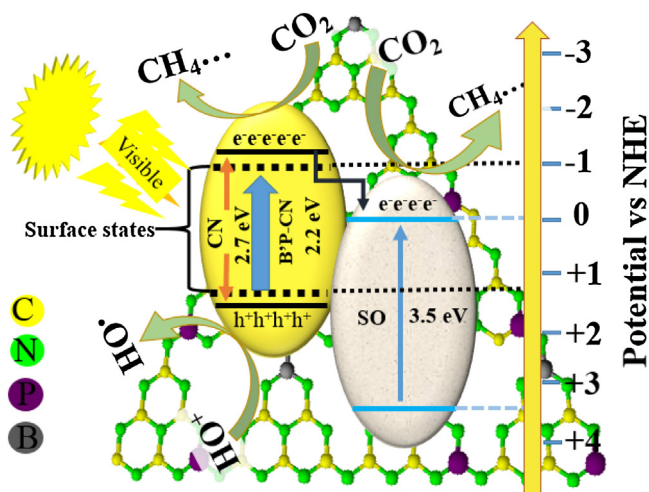
Fig. 6. Mechanism schematic of the photogenerated charge transfer and separation and photocatalytic reactions for CO$_2$ conversion and for pollutant degradation under visible-light irradiation on 6SO/0.12B-0.2P-CN.

as the charge recombination center due to its low energy levels [15]. After coupling with nanocrystalline SO, it is acceptable that the visible-light-excited electrons of doped CN can transfer to SO since the CB level of doped CN lies above the CB bottom of SO [48–50]. This leads to the enhanced charge separation and hence the improved photocatalytic activities. For the resulting 6SO/0.12B-0.2P-CN nanocomposite, it exhibits the highest charge separation and the best photocatalytic performance, up to 550 nm irradiation. This is because that a proper amount of coupled SO is suitable to increase the charge transfer and separation. This is attributed to the extended visible-light absorption from 470 to 550 nm after B-P co-doping, and the promoted charge separation via the dopant-induced surface states and the coupled SO nanoparticles.

4. Conclusions

In summary, we report the synthesis of visible-light driven SO/B'P-CN heterogeneous photocatalysts for effectively conversion of CO$_2$ and degradation of pollutants. It is demonstrated that the resulting SO/B'P-CN nanocomposite exhibits enhanced visible-light activities for CO$_2$ conversion to CH$_4$ from CO$_2$-containing water by ∼9 times, and for phenol and acetaldehyde degradation by ∼7 times, as compared to the bare CN nanosheets, and a large amount of the produced hydroxyl radicals are well responsible for the high photocatalytic activity. This is attributed to the extended visible-light absorption from 460 to 550 nm after B'P co-doping, and

the promoted charge separation via the dopant-induced surface states and the coupled SO. This work will provide feasible routes to synthesize CN-based nanophotocatalysts for efficient solar energy utilization to remedy environmental issues.

Appendix A. Supplementary data

Supplementary data associated with this article can be found, in the online version, at http://dx.doi.org/10.1016/j.apcatb.2016. 08.057.

References

[1] K. Murugan, T.N. Rao, A.S. Gandhi, B.S. Murty, Catal. Commun. 11 (2010) 518–521.
[2] S. Xia, Y. Meng, X. Zhou, J. Xue, G. Pan, Z. Ni, Appl. Catal. B Environ. 187 (2016) 122–133.
[3] J. Qiao, Y. Liu, F. Hong, J. Zhang, Chem. Soc. Rev. 43 (2014) 631–675.
[4] C. Ma, J. Zhou, H. Zhu, W. Yang, J. Liu, Y. Wang, Z. Zou, ACS Appl. Mater. Interfaces 7 (2015) 14628–14637.
[5] S. Zhu, S. Liang, Y. Wang, X. Zhang, F. Li, H. Lin, Z. Zhang, X. Wang, Appl. Catal. B Environ. 187 (2016) 11–18.
[6] S. Muhammad, N. Jitendra, K. Tiwari, K. Christain, Y. Muhammad, K.S. Kim, Environ. Sci. Technol. 47 (2013) 5467–5473.
[7] T. Ohno, T. Higo, N. Murakami, H. Saito, Q. Zhang, Y. Yang, T. Tsubota, Appl. Catal. B Environ. 153 (2014) 309–316.
[8] D.H. Won, C.H. Choi, J. Chung, S.I. Woo, Appl. Catal. B Environ. 158 (2014) 217–223.
[9] N. Sagara, S. Kamimura, T. Tsubota, T. Ohno, Appl. Catal. B Environ. 192 (2016) 193–198.
[10] W. Ho, Z. Zhang, W. Lin, S. Huang, X. Zhang, X. Wang, H. Yu, ACS Appl. Mater. Interfaces 7 (2015) 5497–5505.
[11] M. Humayun, Z. Li, L. Sun, X. Zhang, F. Raziq, A. Zada, Y. Qu, L. Jing, Nanomater 6 (2016) 22–29.
[12] J.L. Bredas, J.E. Norton, J. Cornil, V. Coropceanu, Acc. Chem. Res. 42 (2009) 1691–1699.
[13] Y. He, L. Zhang, B. Teng, M. Fan, Environ. Sci. Technol. 49 (2015) 649–656.
[14] S. Guo, Z. Deng, M. Li, B. Jiang, C. Tian, Q. Pan, H. Fu, Angew. Chem. Int. Ed. 55 (2016) 1830–1834.
[15] F. Raziq, Y. Qu, X. Zhang, M. Humayun, J. Wu, A. Zada, H. Yu, X. Sun, L. Jing, J. Phys. Chem. C 120 (2016) 98–107.
[16] K. Koci, K. Mateju, L. Obalova, S. Krejcikova, Z. Lacny, D. Placha, L. Capek, A. Hospodkova, O. Solcova, Appl. Catal. B Environ. 96 (2010) 239–244.
[17] Y. Zhang, A. Thomas, M. Antonietti, X. Wang, J. Am. Chem. Soc. 131 (2008) 50–51.
[18] C. Alanis, R. Natividad, C. Barrera-Diaz, V. Martinez-Miranda, J. Prince, J.S. Valente, Appl. Catal. B Environ. 140 (2013) 546–551.
[19] F. Raziq, C. Li, M. Humayun, Y. Qu, A. Zada, H. Yu, L. Jing, Mater. Res. Bull. 70 (2015) 494–499.

[20] Y. He, L. Zhang, M. Fan, X. Wang, L.M. Walbridge, Q. Nong, Y. Wu, L. Zhao, Sol. Energy Mater. Sol. C 137 (2015) 175–184.
[21] P. Babu, R. Kumar, P. Linga, Environ. Sci. Technol. 47 (2013) 13191–13198.
[22] F. Alexandra, S. Justus-von, S. Clemens-von, C.S. Torsten, Environ. Sci. Technol. 47 (2013) 9959–9964.
[23] L. Jing, W. Zhou, G. Tian, H.Fu. Chem. Soc. Rev. 42 (2013) 9509–9549.
[24] J. Xu, L.W. Zhang, R. Shi, Y.F. Zhu, J. Mater. Chem. A 1 (2013) 14766–14772.
[25] Y. Wang, H.R. Li, J. Yao, X.C. Wang, M. Antonietti, Chem. Sci. 2 (2011) 446–450.
[26] M. Humayun, A. Zada, Z. Li, M. Xie, X. Zhang, Y. Qu, F. Raziq, L. Jing, Appl. Catal. B Environ. 180 (2016) 219–226.
[27] Y. Zhang, T. Mori, J. Ye, M. Antonietti, J. Am. Chem. Soc. 132 (2010) 6294–6295.
[28] Y. Zhu, T. Ren, Z. Yuan, ACS Appl. Mater. Interface 7 (2015) 16850–16856.
[29] A. Thomas, A. Fischer, F. Goettmann, M. Antonietti, J. Mater. Chem. 18 (2008) 4893–4908.
[30] Y. Li, J. Zhang, Q. Wang, Y. Jin, D. Huang, Q. Cui, G. Zou, J. Phys. Chem. B 114 (2010) 9429–9434.
[31] Y. Wang, H. Li, J. Yao, X. Wang, M. Antonietti, Chem. Sci. 2 (2011) 446–450.
[32] Y. Zhou, L. Zhang, J. Liu, X. Fan, B. Wang, Min Wang, W. Ren, J. Wang, M. Li, J. Shi, J. Mater. Chem. A 3 (2015) 3862–3867.
[33] X.G. Ma, Y.H. Lv, J.Y. Xu, F.R.Q. Zhang, Y.F. Zhu, J. Phys. Chem. C 116 (2012) 23485–23493.
[34] Y. Zhou, L. Zhang, J. Liu, X. Fan, B. Wang, Min. Wang, W. Ren, J. Wang, M. Li, J. Shi, J. Mater. Chem. A. 3 (2015) 3862–3867.
[35] G. Zhao, X. Huang, F. Fina, G. Zhang, T.S. Irvine, Catal. Sci. Technol. 5 (2015) 3416–3422.
[36] S. Zhou, Y. Liu, J. Li, Y. Wang, G. Jiang, Z. Zhao, D. Wang, A. Duan, J. Liu, Y. Wei, Appl. Catal. B Environ. 159 (2014) 20–29.
[37] Y. Wang, X. Bai, H. Qin, F. Wang, Y. Li, X. Li, S. Kang, Y. Zuo, L. Cui, ACS Appl. Mater. Interface 8 (2016) 17212–17219.
[38] M. Li, L. Zhang, X. Fan, Y. Zhou, M. Wu, J. Shi, J. Mater. Chem. A 3 (2015) 5189–5196.
[39] J. Lin, Z. Pan, X. Wang, ACS Sust. Chem. Eng. 2 (2014) 353–358.
[40] L. Shi, T. Wang, H. Zhang, K. Chang, J. Ye, Adv. Funct. Mater. 25 (2015) 5360–5367.
[41] H. Zhou, P. Li, J. Liu, Z. Chen, L. Liu, D. Dontsova, R. Yan, T. Fan, D. Zhang, J. Ye, Nano Energy 25 (2016) 128–135.
[42] W.J. Ong, L.L. Tan, S.P. Chai, S.T. Yong, A.R. Mohamed, Nano Energy 13 (2015) 757–770.
[43] C. Li, F. Raziq, C. Liu, Z. Li, L. Sun, L. Jing, Appl. Surf. Sci. 358 (2015) 240–245.
[44] C. Liu, C. Li, X. Fu, F. Raziq, Y. Qu, L. Jing, RSC Adv. 5 (2015) 37275–37280.
[45] Y.H. Lin, D.J. Wang, Q.D. Zhao, M. Yang, Q.L. Zhang, J. Phys. Chem. B 108 (2004) 3202–3206.
[46] Y. Luan, L. Jing, M. Xie, X. Shi, X. Fan, Y. Cao, Y. Feng, Phys. Chem. Chem. Phys. 14 (2012) 1352–1359.
[47] X.C. Wang, S. Blechert, M. Antonietti, ACS Catal. 2 (2012) 1596–1606.
[48] Jin. Mao, T. Peng, X. Zhang, K. Li, L. Ye, L. Zan, Catal. Sci. Technol. 3 (2013) 1253–1260.
[49] L. Jing, X. Sun, W. Cai, Z. Xu, Y. Du, H. Fu, J. Phys. Chem. Solids 64 (2003) 615–623.
[50] G.H. Dong, L.Z. Zhang, J. Phys. Chem. C 117 (2013) 4062–4068.